Check for updates

Accelerated alkaline hydrogen evolution on M(OH)$_x$/M-MoPO$_x$ (M = Ni, Co, Fe, Mn) electrocatalysts by coupling water dissociation and hydrogen ad-desorption steps†

Lishan Peng, [ID] ‡[a] Mansheng Liao,‡[a] Xingqun Zheng,‡[a] Yao Nie,[b] Ling Zhang,[a] Minjie Wang,[a] Rui Xiang,[a] Jian Wang,[a] Li Li*[a] and Zidong Wei [ID] *[a]

Developing efficient and cheap electrocatalysts for the alkaline hydrogen evolution reaction is still a big challenge due to the sluggish water dissociation kinetics as well as poor M–H$_{ad}$ energetics. Herein, hydroxide modification and element incorporation have been demonstrated to realize a synergistic modulation on a new class of M(OH)$_x$/M-MoPO$_x$ catalysts for accelerating water dissociation and hydrogen ad-desorption steps in the HER. Theoretical and experimental results disclosed that *in situ* modification with hydroxide endowed M(OH)$_x$/M-MoPO$_x$ with a strong ability to dissociate water, and meanwhile, oxygen incorporation effectively optimized the M–H$_{ad}$ energetics of the NiMoP catalyst. Moreover, the interaction between M(OH)$_x$ and M-MoPO$_x$ components in M(OH)$_x$/M-MoPO$_x$ further enhances their ability to catalyze the two elementary steps in alkaline hydrogen evolution, providing a wide avenue for efficiently catalyzing hydrogen evolution. In general, the optimized Ni(OH)$_2$/NiMoPO$_x$ catalyst exhibits excellent alkaline HER activity and durability, superior to the state-of-the-art Pt/C catalyst when the overpotential exceeds 65 mV.

Introduction

Hydrogen has been extensively researched as an alternative fuel source to fossil fuels. Water electrolysis is an appealing, but challenging method for large-scale production of H$_2$. In a water-alkali electrolyser, there are two half-cell reactions occurring at the cathode and anode, *i.e.* the hydrogen evolution reaction (HER) and the oxygen evolution reaction (OER). The kinetics of these two electrochemical reactions under typical operation conditions are inherently slow, which necessitates the use of catalysts with high activity and stability to reduce electricity consumption.[1–4] Nowadays, the most effective HER catalysts are Pt-based metals, but their industrial application is limited by their scarcity and high cost. Although some studies have been conducted to replace Pt with Ru compounds (that are relatively low in cost), the intrinsic limitation of noble metals has still not been overcome completely.[5,6] Thus, it is especially important to use highly active HER electrocatalysts derived from low-cost materials.

In recent few years, abundant non-noble metal-based materials have been developed as promising electrocatalysts for hydrogen evolution under alkaline conditions.[7,8] Among these transition metal catalysts, molybdenum-based compounds,[9] such as alloys,[10] carbides,[11–15] chalcogenides,[16–18] and phosphides,[19–21] have recently attracted significant research interest due to their desired chemical and physical properties. For example, as a prototypical model, MoS$_2$ is the first reported transition metal-based HER catalyst, in which only the surface edges are catalytically active.[22–24] Unlike MoS$_2$, which only shows HER activity at surface edges, all the sites of bulk MoP show high HER activity. Calculations of P sites on MoP indicate that P acts like a 'hydrogen deliverer' as hydrogen adsorbs on P at low coverage whilst it desorbs at high coverage.[25,26] Accordingly, molybdenum phosphides usually exhibit higher HER current density than MoS$_2$, as more active sites are available for the intensive electrocatalytic reaction. However, even though these MoP-based catalysts have abundant active sites for catalyzing protons to hydrogen, their HER activities are still unsatisfactory, especially in alkaline solution.

Under alkaline conditions, the HER process inevitably undergoes the first water dissociation step (Volmer step), because there are few protons existing in alkaline solutions.[27,28] In 2012, Markovic *et al.* probed the surface HER reactivity of the

[a]The State Key Laboratory of Power Transmission Equipment & System Security and New Technology, Chongqing Key Laboratory of Chemical Process for Clean Energy and Resource Utilization, School of Chemistry and Chemical Engineering, Chongqing University, Chongqing 400044, China. E-mail: zdwei@cqu.edu.cn; liliracial@cqu.edu.cn

[b]College of Chemistry, Chongqing Normal University, Chongqing 400047, China

† Electronic supplementary information (ESI) available. See DOI: 10.1039/c9sc04603h

‡ These authors contributed equally to this work.

materials with near-optimal M–H_{ad} energetics (such as Pt) and found that it can be enhanced by modifying them with more efficient active sites (such as 3d metal hydroxides) for water molecule dissociation.[29] Recently, our group has found that there is a strong interaction occurring at the interface of Ni@Ni(OH)$_2$–Pd, which is effective for catalysing hydrogen generation in alkaline solution compared with the pure Pd catalyst.[30] With this in mind, we speculate that two types of active sites are required for efficient alkaline hydrogen evolution, *i.e.*, one with optimized M–H_{ad} energetics (ΔG(H)) and another with the capability of accelerating the dissociation of water. However, all the above-mentioned HER catalysts contain noble metals (*e.g.* Pt and Pd) which seem to act as indispensable parts for the high HER activity. Pure metal oxides or hydroxides are generally considered as HER inactive materials, although they facilitate the water dissociation step.[31,32] Such strong dependency on noble metals is undesirable for future massive applications. Therefore, achieving a satisfactory synergism in accelerating both water dissociation and hydrogen ad-desorption (*i.e.* optimal M–H_{ad} energetics) steps on a non-noble material is urgent but challenging for an efficient HER.

Based on the above observation, we put forward that hydroxide modification and element incorporation can help realize a synergistic modulation for accelerating both water dissociation and hydrogen ad-desorption steps in the HER. And a new class of noble-metal free catalysts, M-MoPO$_x$-based nanomaterials *in situ* modified with hydroxide species on the surface (M(OH)$_x$/M-MoPO$_x$, M = Ni, Co, Fe, Mn), served as a platform to elaborate our proposed view. Combining experiments with DFT calculations, we demonstrated that on the one hand, hydroxide modification generates more active sites in catalysts for water dissociation, thus accelerating the Volmer step during the HER process. On the other hand, oxygen incorporation can regulate the electronic structure of M-MoP, resulting in modulated M–H_{ad} energetics. More interestingly, we also revealed that the interaction between M(OH)$_x$ and M-MoPO$_x$ further enhances their catalytic abilities, *i.e.*, M(OH)$_x$ and M-MoPO$_x$ components in M(OH)$_x$/M-MoPO$_x$ catalysts exhibit greater abilities in catalysing water dissociation and hydrogen ad-desorption steps than their corresponding single component catalysts, respectively. Benefiting from the hydroxide modification, element incorporation and component interaction, efficient HER activity in an alkaline environment was achieved, proving the validity of coupling water dissociation and hydrogen ad-desorption steps for efficient alkaline hydrogen evolution.

Results and discussion

The typical preparation procedure of the hydroxide species modified M-MoPO$_x$ based nanomaterials is schematically described in Scheme S1.† Taking Ni(OH)$_2$/NiMoPO$_x$/NF as the representative example, a flower-like structure composed of regular NiMoO$_4$ nanocuboids on the surface of Ni foam was first acquired *via* a facile and scalable hydrothermal method.[15] Field-emission scanning electron microscopy (FESEM) indicates that the NiMoO$_4$ nanocuboids uniformly grown on Ni foam have an

average width of about 300 nm and a very smooth surface (Fig. S1a†), and the 3D-network structure of Ni foam is of great benefit for loading the active species. Then the as-prepared NiMoO$_4$/NF was transformed into NiMoPO$_x$/NF by phosphatizing with NaH$_2$PO$_2$ at 400 °C for 2 h under an Ar gas flow. No obvious change in the morphology can be observed when NiMoO$_4$/NF was converted into NiMoPO$_x$/NF (Fig. S1b–d†), while the crystal structure changes from the high-crystallinity NiMoO$_4$ phase (JCPDS no. 86-0361) to the Ni$_2$P$_4$O$_{12}$ phase (JCPDS no. 76-1557) (Fig. 1b). As depicted in Fig. S1e,† the NiMoPO$_x$ nanocuboids are composed of numerous nanocrystallites with a small size of about 10 nm, uniformly embedded in the amorphous phase. High-resolution TEM (HRTEM) confirmed the crystalline nature of the nanocrystallites. The lattice fringes with an interplanar distance of 0.23 nm in Fig. S1f† correspond to the (−133) planes of Ni$_2$P$_4$O$_{12}$. Energy dispersive X-ray spectra (Fig. S1g†) show that Ni, Mo, P and O are distributed over the NiMoPO$_x$ nanocuboids. The atomic contents of Ni, Mo, P and O are 12.22, 13.66, 14.33 and 59.80, respectively (Fig. S1h†), and the exact chemical formula of MMoPO$_x$ is NiMo$_{1.12}$P$_{1.17}$O$_{4.89}$. Considering the P-XRD results and EDX-mapping results, it can be speculated that the NiMoPO$_x$ material contains crystalline Ni$_2$P$_4$O$_{12}$ and an amorphous Mo-containing compound.

After electrochemical transformation in 1 M NaOH, tiny and flexible Ni(OH)$_2$ nanosheets were generated through redox of Ni$_2$P$_4$O$_{12}$, and were uniformly attached to the surface of pre-synthesized NiMoPO$_x$ nanocuboids to produce Ni(OH)$_2$/NiMoPO$_x$/NF hybrid nanocuboids (named Ni(OH)$_2$/NiMoPO$_x$). Fig. S2a† displays the CV curves at different scans for the presented NiMoPO$_x$/NF. Obviously, the current density of NiMoPO$_x$/NF continuously increases with CV scans until 8000 cycles, as well as the area of the redox zone (−0.15 to 0.2 V). These results reveal that the catalytic properties of NiMoPO$_x$/NF change constantly with the CV scans. On the basis of the general electrochemical redox states of elements under potential bias,[33] it is speculated that the Ni species on the surface of NiMoPO$_x$/NF varied during electrochemical activation. The growing area of the redox zone implies that more Ni species were involved in the reaction during the redox switching scan. In addition, the existence of PO$_4^{3-}$ ions in the electrolytes used for electrochemical activation of M-MoPO$_x$ was detected by UV-vis-NIR spectroscopy (Fig. S3a†). XRD results show that a crystal structure transition occurred after 8000 cycles, as crystalline Ni$_2$P$_4$O$_{12}$ disappeared and NiMoPO$_x$/NF became an amorphous structure (Fig. 1b). It has been reported that Co-based phosphate would leach out and transform into hydroxide during the electrochemical redox process in alkaline solution,[34] which shows us that an *in situ* transformation of crystalline Ni$_2$P$_4$O$_{12}$ into amorphous Ni(OH)$_2$ occurred on the NiMoPO$_x$/NF surface *via* the following pathways:

$$\mathrm{Ni_2P_4O_{12} + 12OH^- = 2Ni(OH)_2 + P_4O_{12}^{4-} + 4H_2O} \quad (1)$$

Electron microscopy observations together with X-ray photon spectroscopy (XPS) of NiMoPO$_x$/NF prove the evolution of local structures during electrochemical activation. SEM
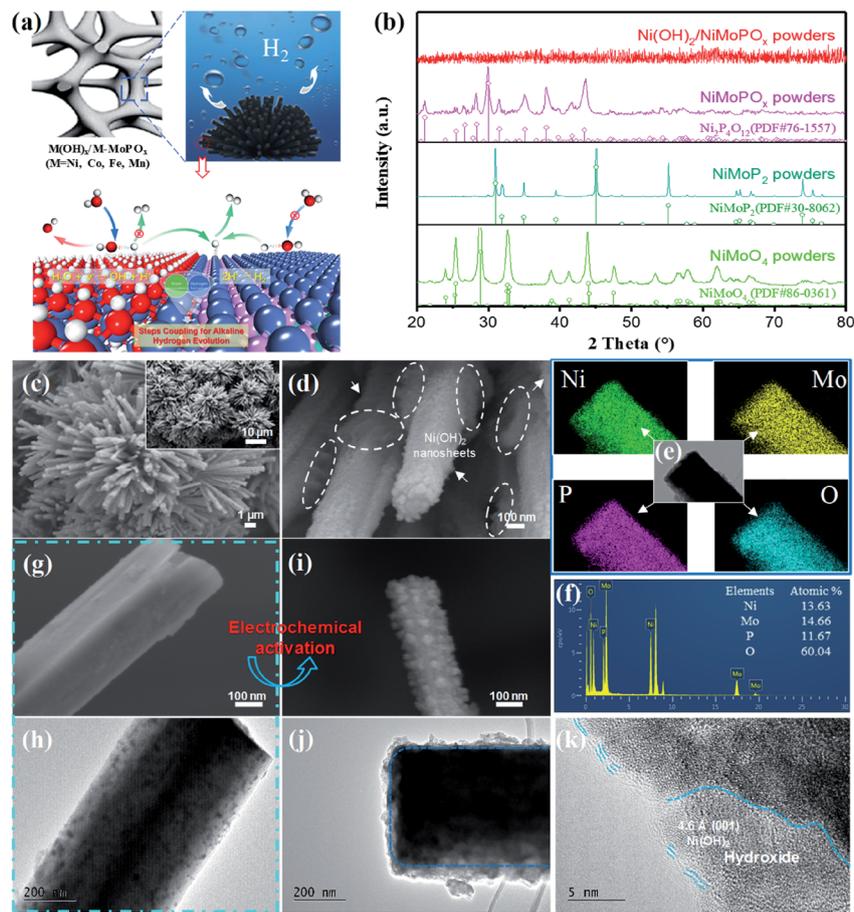
Fig. 1 (a) Schematic illustration of the microstructure of $M(OH)_x/M-MoPO_x$. (b) P-XRD patterns of $NiMoO_4$, $NiMoPO_x$ and $Ni(OH)_2/NiMoPO_x$ powders scraped from Ni foam. (c and d) SEM images, (e) elemental mapping and (f) EDX spectrum of $Ni(OH)_2/NiMoPO_x$. Morphology comparison of (g and h) $NiMoPO_x$ and (i and j) $Ni(OH)_2/NiMoPO_x$ on the same scale. (k) HR-TEM image of $Ni(OH)_2/NiMoPO_x$.

images (Fig. 1c and d) reveal that the morphology of $NiMoPO_x$/NF is maintained in activated $Ni(OH)_2/NiMoPO_x$/NF, while a large number of nanosheets appear on the surface of $NiMoPO_x$/NF. The diameter of $Ni(OH)_2/NiMoPO_x$/NF nanocuboids gets smaller and their surface becomes more rough than that of $NiMoPO_x$/NF (Fig. 1g–j). Although the mapping images (Fig. 1e) show that the elements are still uniformly distributed over the nanocuboids, the decreased atomic content of the P element measured by EDX spectroscopy (Fig. 1f) further reveals the dissolution of P-species during electrochemical activation. The HR-TEM image (Fig. 1k) verifies the existence of newly formed amorphous $Ni(OH)_2$ nanosheets with a short-order (001) plane on the $Ni(OH)_2/NiMoPO_x$/NF surface and the disappearance of crystalline $Ni_2P_4O_{12}$ nanoparticles inside the catalyst. The variation of element valences and their contents on the catalyst surface was analysed by XPS (Fig. 2). A higher Ni content in XPS than in EDX in contrast to the lower P and Mo contents in XPS than in EDX (Table S1,† Fig. 1f) demonstrates the relatively outer position of Ni and inner position of P and Mo in the transformed nanostructure. Ni species have three states (Fig. 2a), *i.e.* Ni^0 (851.8 eV), Ni^{2+} (855.9 eV), and Ni^{3+} (858.5 eV). Compared with $NiMoPO_x$/NF, $Ni(OH)_2/NiMoPO_x$/NF has a higher content of Ni^{2+} species and a decreased Ni^{3+} content.

Meanwhile, an additional peak of OH^- groups is observed in the O 1s spectrum of $Ni(OH)_2/NiMoPO_x$/NF, indicating the new formation of $Ni(OH)_2$ on the surface of the activated catalysts (Fig. 2d). The sharply decreased P and Ni^{3+} content together
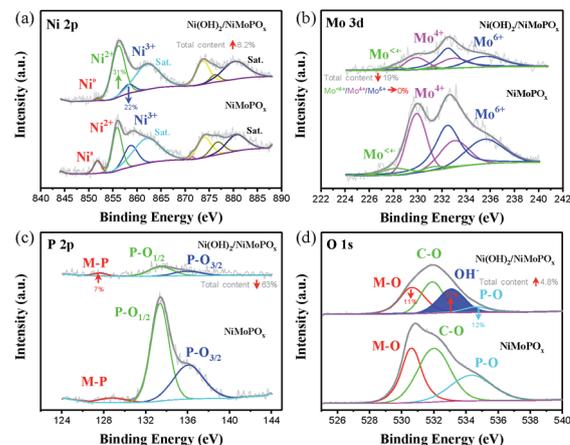

Fig. 2 XPS spectra of $NiMoPO_4$ and $Ni(OH)_2/NiMoPO_x$; (a) Ni 2p region, (b) Mo 3d region, (c) P 2p region and (d) O 1s region.

with the intensively increased Ni^{2+} content measured by XPS further confirms that the $Ni_2P_4O_{12}$ first leached out and the Ni ions are then re-deposited to form the hydroxide during the electrochemical redox process. The overall element contents of $Ni(OH)_2/NiMoPO_x$ in Fig. 1f reveal that the core component is amorphous $NiMoPO_x$. The relative contents of Mo species with different valences are stably retained in the $Ni(OH)_2/NiMoPO_x/$ NF hybrids, verifying that the amorphous $NiMoPO_x$ below the thin $Ni(OH)_2$ layer retains its original state after electrochemical activation. Based on the above evidence, $Ni(OH)_2/NiMoPO_x/NF$ is shown to be composed of amorphous $NiMoPO_x$ in the core and a thin $Ni(OH)_2$ layer on its surface. Beyond $Ni(OH)_2/NiMoPO_x/NF$, a series of 3D-nanocuboid hybrids composed of other 3d metals (Co, Fe, and Mn) were obtained. SEM images show that $CoMoPO_x/NF$ and $MnMoPO_x/NF$ also have a nanocuboid-like structure while the structure of $FeMoPO_x/NF$ is nanoflake-like (Fig. S4†). The element valences and contents of $M-MoPO_x$ and activated $M(OH)_x/M-MoPO_x$ were measured by XPS (Fig. S4–S7 and Table S2†). The variation trend of element content in $M-MoPO_x$ and corresponding $M(OH)_x/M-MoPO_x$ is similar to that of $NiMoPO_x$, demonstrating the universality of electrochemical activation in modulating the catalyst surface structure.

The catalytic performance of the synthesized electrocatalysts in the alkaline HER was evaluated in N_2-saturated 1.0 M NaOH. The polarization curves of $Ni(OH)_2/NiMoPO_x/NF$ along with those of $NiMoPO_x/NF$, $NiMoP_2/NF$, $NiMoO_4/NF$, Ni foam, and commercial Pt/C loaded on NF (20 wt% Pt/C/NF) without iR correction are shown in Fig. 3a. $NiMoP_2/NF$ exhibits a good HER activity, while Ni foam exhibits relatively poor HER activity, and $NiMoO_4/NF$ and $Ni(OH)_2/NF$ are even worse. As expected, the O incorporation greatly improves the HER performance of $NiMoPO_x/NF$ due to optimized hydrogen binding energy (H_{ad}).[35] Furthermore, the generation of $Ni(OH)_2$ on the $NiMoPO_x$ nanocuboids results in a sharply improved HER reactivity, which even outperformed that of the benchmark Pt/C. In the iR corrected polarization curves (Fig. 3b), $Ni(OH)_2/NiMoPO_x/NF$ exhibits a rapid enhancement of the cathodic current along with negative potential and surpasses the current density of Pt/C when the overpotential exceeds 65 mV. Moreover, to drive a current density of 10 mA cm^{-2}, $Ni(OH)_2/NiMoPO_x/NF$ needs an extremely low overpotential of 51 mV, which is markedly lower than that of $NiMoO_4/NF$ (234 mV), $NiMoPO_x/NF$ (77 mV), and the most advanced HER electrocatalysts reported recently, such as $Ni(OH)_2/MoS_2$ (80 mV),[36] $NiCo_2P_x/CF$ (58 mV),[37] Cu NDs/ Ni_3S_2 NTs–CFs (128 mV)[38] and CoMoP@C (81 mV)[39] (more details in Table S6†). To obtain a larger cathodic current density of 100 mA cm^{-2}, $Ni(OH)_2/NiMoPO_x/NF$ needs an overpotential of 72 mV, approaching half the overpotential of 20% Pt/C/NF (154 mV, Table S3†). Such an excellent HER activity of $Ni(OH)_2/NiMoPO_x/NF$ is impressive and shows its potential for industrial application.

The Tafel plots of these electrocatalysts were measured to provide a deep insight into the HER reaction pathways on the electrocatalysts (Fig. 3c, Table S3†). The Tafel slope of $Ni(OH)_2/$ $NiMoPO_x/NF$ is 33 mV dec^{-1}, much lower than that of Ni foam (140 mV dec^{-1}), $NiMoO_4/NF$ (101 mV dec^{-1}), $NiMoPO_x/NF$
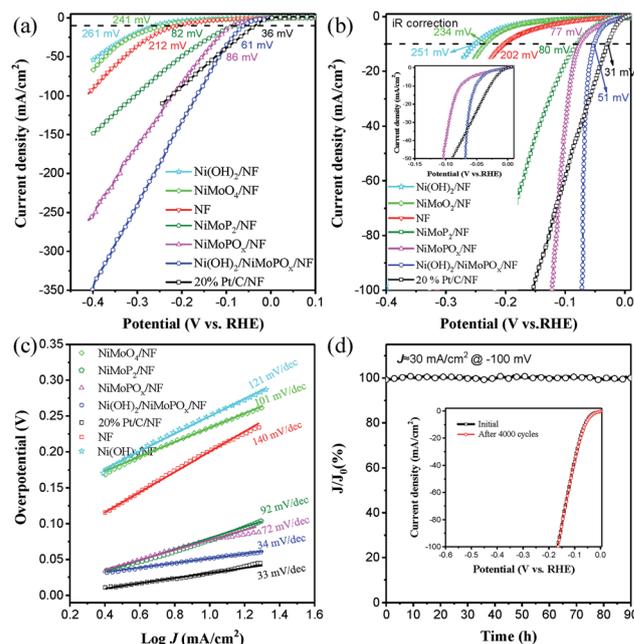

Fig. 3 (a) LSV curves, (b) LSV curves with iR correction and (c) Tafel slopes of $NiMoO_x/NF$, $NiMoPO_x/NF$, $Ni(OH)_2/NiMoPO_x/NF$, 20% Pt/C/ NF and NF with 5 mV s^{-1} in 1 M NaOH. (d) Chronopotentiometry curve of $Ni(OH)_2/NiMoPO_x/NF$ at a constant potential of −100 mV for 90 hours. The inset in (d) is the LSV curves of $Ni(OH)_2/NiMoPO_x/NF$ before and after 4000 CV scans at −0.3 V ~ +0.2 V vs. RHE at 100 mV s^{-1}.

(72 mV dec^{-1}), and 20 wt% Pt/C/NF (34 mV dec^{-1}). Such a low value of the Tafel slope suggests that the HER kinetics on $Ni(OH)_2/NiMoPO_x/NF$ is determined by the Tafel step rather than by the Volmer step. Furthermore, the electrochemical impedance spectroscopy results (EIS, Fig. S8a†) of $Ni(OH)_2/$ $NiMoPO_x/NF$ further show a faster HER kinetics process than that on the $NiMoPO_x/NF$. Compared with the $NiMoPO_x/NF$, which undergoes the Volmer–Heyrovsky mechanism during the HER process, it is easy to infer that the formation of $Ni(OH)_2$ on its surface significantly accelerates the HER reaction kinetics by optimizing the water dissociation step. In addition, the electrochemical specific surface area (ECSA, Fig. S8b and S9†) of $Ni(OH)_2/NiMoPO_x/NF$ is 56.4 mF cm^{-2}, which is similar to that of $NiMoPO_x/NF$ (48.6 mF cm^{-2}), revealing that the enhancement of the HER activity is not attributed to the enlargement of the ECSA, but the improvement of the intrinsic activity.

Stability is another important evaluation index for the performance of catalysts in practical applications, especially in strongly alkaline media. The long-term stability of the best catalyst $Ni(OH)_2/NiMoPO_x/NF$ was studied by continuous electrolysis at an overpotential of 100 mV for over 90 h. A steady current curve without notable degradation was observed during the 90 h aging test in an alkaline environment (Fig. 3d). Besides, the LSV curves (inset in Fig. 3d) of $Ni(OH)_2/NiMoPO_x/NF$ show almost no change after 4000 CV cycles, revealing that $Ni(OH)_2/$ $NiMoPO_x/NF$ possesses good corrosion resistance in a wider potential region. The $Ni(OH)_2/NiMoPO_x/NF$ also exhibits a comparable HER activity and stability to the industrial

PtRuNiP/Ni electrode when integrated into a practical water electrolyzer (Fig. S10†). It is not difficult to understand the excellent stability of $Ni(OH)_2/NiMoPO_x/NF$: (i) the unique three-dimensional flower-like structures comprising regular nano-cuboids can provide patulous architectures and open spaces that are beneficial to promote the release of generated gas bubbles. (ii) The *in situ* growth technology enhances the mechanical adhesion between catalysts and substrates. (iii) Moreover, the hydroxides formed on the surface of the catalyst and appropriate phosphate species can serve as protective agents to enhance the stability of $Ni(OH)_2/NiMoPO_x/NF$ in alkaline solution.[40,41]

In order to confirm the synergistic effect of the hybrid structure for coupling the water dissociation and hydrogen ad-desorption processes during the alkaline HER, we studied the structural properties and HER activities of $NiMoPO_x$, $Ni(OH)_2/NiMoPO_x$ and $Ni(OH)_2/NiMoPO_x$-acid in 1 M $HClO_4$ and 1 M NaOH (Fig. 4a, b and S11†). As for the Raman spectrum of the $NiMoPO_x$ sample, the absorption bands at ~200, 330, 710, 880 and 960 cm^{-1} can be assigned to the phosphomolybdate anion.[42,43] After electrochemical activation, two new broad bands at 365 and 470 cm^{-1} appear, corresponding to the $E_g(T)$ mode of the Ni-OH lattice vibration and the $A_{1g}(T)$ mode due to vNi-OH, respectively.[44,45] The band at 550 cm^{-1} is consistent with the structural defects.[46,47] These results indicate the generation of amorphous $Ni(OH)_2$ on the surface of $NiMoPO_x$ during electrochemical activation. The band of P–O–P for $Ni(OH)_2/NiMoPO_x$ is red-shifted in comparison with that for the $NiMoPO_x$, due to the interaction between $Ni(OH)_2$ and $NiMoPO_x$. The $Ni(OH)_2/NiMoPO_x$ was then treated by acid

etching in 0.5 M H_2SO_4 to remove the generated $Ni(OH)_2$ on its surface and its Raman spectrum changes back to that of the $NiMoPO_x$ sample, revealing that only the surfacial component of $NiMoPO_x$ changes but the inside does not change during electrochemical activation.

It should be pointed out that the HER activity at high pH values is determined using $M–H_{ad}$ bond strength and the energy required for water dissociation simultaneously. While in acid electrolyte, the HER activity can only be determined using $M–H_{ad}$ bond strength, as the H protons are abundant.[48] Therefore, the alkaline activities of HER catalysts are always worse than their acid activities due to the additional energy required for water dissociation. As shown in Fig. 4b, the observed activities of the three catalysts in alkaline solutions are obviously lower than those in acid solutions. The alkaline HER activity of $Ni(OH)_2/NiMoPO_x$ is significantly superior to that of $NiMoPO_x$ in alkaline electrolyte, and is similar to that of $NiMoPO_x$ in acid electrolyte. When the generated $Ni(OH)_2$ on the surface of $Ni(OH)_2/NiMoPO_x$ is removed by acid etching, the HER activity of $Ni(OH)_2/NiMoPO_x$-acid in both acid and alkaline electrolytes reduces back to that of the original $NiMoPO_x$. These results confirm that the obstruction of water dissociation for $NiMoPO_x$ in alkaline electrolyte can be effectively resolved by the generated $Ni(OH)_2$.

The HER activities of other 3d $M(OH)_x/M$-$MoPO_x$ (M = Ni, Co, Fe, Mn) hybrids were systemically investigated to confirm the universality of coupling water dissociation and hydrogen ad-desorption for excellent alkaline HER activity. The HER polarization curves in 1 M NaOH are shown in Fig. 4c. A clear alkaline HER activity trend is observed in the order of Fe < Mn < Co < Ni for both M-$MoPO_x$ catalysts and the derived $M(OH)_x/M$-$MoPO_x$ hybrids. Besides, all these derived $M(OH)_x/M$-$MoPO_x$ hybrids exhibit an obvious improvement in activity to different degrees compared with the original M-$MoPO_x$ catalysts (Fig. 4d). This result reveals that the *in situ* formed hydroxide is commonly useful for improving the HER activity of these M-$MoPO_x$-based catalysts. The Tafel slopes, EIS spectra, ECSA and ECSA-normalized HER polarization curves of these catalysts were further measured (Fig. S12–S14, Table S4†). The Tafel slopes of $Ni(OH)_2/NiMoPO_x/NF$ and $Co(OH)_2/CoMoPO_x/NF$ sharply reduce from around 70 mV dec^{-1} to below 40 mV dec^{-1} as well as that of $Mn(OH)_x/MnMoPO_x/NF$, revealing that the sluggish Volmer step (*i.e.* water dissociation) was thoroughly accelerated by the newly formed $M(OH)_x$ on the catalyst surface. The relatively larger Tafel slope of $Fe(OH)_x/FeMoPO_x/NF$ is ascribed to the very strong adsorption of the Fe based hydroxide. The much smaller reaction resistances (R_{ct}) of these $M(OH)_x/M$-$MoPO_x$ catalysts further confirm the faster HER kinetics process on the hybrid catalysts. Therefore, it is speculated that the hybridized $M(OH)_x$ side is favourable for producing H* and OH$^-$ *via* accelerating the water dissociation step ($H_2O \rightarrow H^* + OH^- + e^-$).[49,50] On the other hand, all these M-$MoPO_x$ catalysts are weak in water dissociation, and the distinct difference in their HER activities should be ascribed to the ability of catalyzing the H_2 ad-desorption step. Despite the strong water dissociation ability of $Ni(OH)_2$, the poor HER activity of the $Ni(OH)_2/NF$ compared with that of $NiMoPO_x$ and $Ni(OH)_2/NiMoPO_x$ further confirms
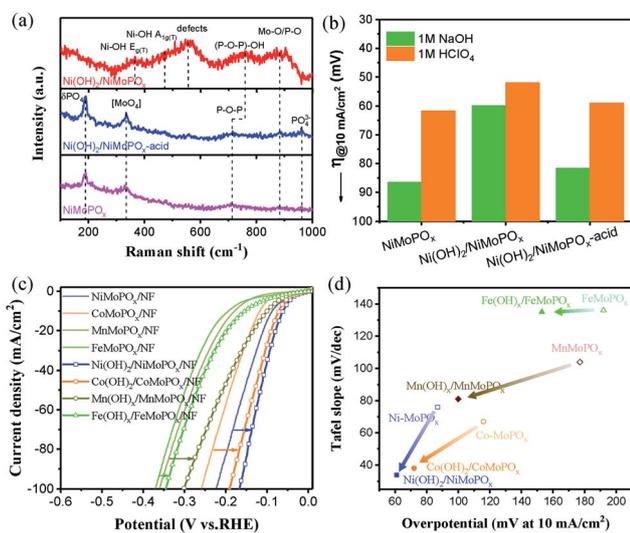

Fig. 4 (a) Raman spectra and (b) comparison between activities for the HER, expressed as the overpotential required for a 10 mA cm^{-2} current density, in 1 M $HClO_4$ and 1 M NaOH of the $NiMoPO_x$, $Ni(OH)_2/NiMoPO_x$ and $Ni(OH)_2/NiMoPO_x$-acid; (c) LSV curves of M(Ni, Co, Fe, Mn)-$MoPO_x/NF$ and their activated $M(OH)_2/M$-$MoPO_x/NF$ electrodes without iR correction; (d) comparison with M(Ni, Co, Fe, Mn)-$MoPO_x/NF$ electrocatalysts before and after electrochemical activation in alkaline solutions.

the crucial role of the hydrogen ad-desorption step in the overall HER process. Based on the experimental results above, we can easily assume that superior alkaline HER catalysts should be capable of catalysing both water dissociation and hydrogen ad-desorption steps efficiently.

To gain further insights into the origin of the hybrid heterostructure for the excellent HER activity, DFT calculations on the H$_2$O dissociation step (ΔG(H$_2$O), Volmer step) and the H ad-desorption step (ΔG(H), Tafel step) were performed (Fig. 5a). The energy change in the Volmer reaction (ΔG_R, Fig. 5b) for Ni(OH)$_2$/NiMoPO$_x$ (0.60 eV) is lower than that of Ni*MoPO$_x$ (1.31 eV) and Ni*(OH)$_2$ (1.38 eV), revealing that the Ni*(OH)$_2$/NiMoPO$_x$ hybrid is more favourable for H$_2$O dissociation thermodynamically. Moreover, the water dissociation kinetic energy barrier (ΔG_{TS}) of Ni*(OH)$_2$/NiMoPO$_x$ dramatically decreases from the 2.89 eV of Ni*MoPO$_x$ to 1.01 eV, suggesting that the sluggish Volmer step on NiMoPO$_x$ was greatly accelerated after the *in situ* generation of the Ni(OH)$_2$ component. As for the concomitant Tafel step (Fig. 5c), the Ni(OH)$_2$ has a very negative ΔG(H) (−0.37 eV), indicating a very high H adsorption strength, while all these NiMoP based catalysts present modulated ΔG(H) closer to the thermoneutral. The ΔG(H) of Ni*MoPO$_x$ is further decreased by 0.04 eV when O atoms are doped into the Ni*MoP, suggesting that the incorporation of O can modulate the H adsorption on the surface of the NiMoP catalyst. Interestingly, the final Ni(OH)$_2$/Ni*MoPO$_x$ obtains an optimal ΔG(H) of 0.14 eV, which is even close to the absolute value of ΔG(H) for Pt* (−0.09 eV).[51,52] Note that the water dissociation kinetic energy barrier (ΔG_{TS}) and hydrogen adsorption free energy (ΔG(H)) of Ni(OH)$_2$/NiMoPO$_x$ are superior to the ΔG_{TS} of pure Ni(OH)$_2$ and the ΔG(H) of pure NiMoPO$_x$. This result reveals that the interaction between the two components in Ni(OH)$_2$/NiMoPO$_x$ could further enhance their catalytic ability, *i.e.*, the Ni(OH)$_2$ and NiMoPO$_x$ components in Ni(OH)$_2$/NiMoPO$_x$ catalysts possess greater ability to catalyze the water dissociation and hydrogen ad-desorption steps, respectively. Thus, the two types of active sites required for alkaline hydrogen evolution coexist adjacently in the Ni(OH)$_2$/NiMoPO$_x$ catalysts, providing a new and smoother mechanism for hydrogen evolution *via* the synergy of Ni(OH)$_2$ and NiMoPO$_x$ components. That is, H* is formed by H$_2$O* dissociation on the metal hydroxide first and then transferred to the adjacent NiMoPO$_x$ sites to form H$_2$. These results combined with experimental observations reveal that the excellent HER activity of Ni(OH)$_2$/NiMoPO$_x$ is attributed to the synergistic effect in the hybrid components.

Conclusions

In summary, synergistic modulation of both Volmer and Tafel steps for alkaline hydrogen evolution was achieved in NiMoP nanocuboids by hydroxide modification and element incorporation. By *in situ* modification with the hydroxide, the HER catalysts are endowed with the strong ability to dissociate water. Besides, the M–H$_{ad}$ energetics of the NiMoP catalyst was optimized by oxygen incorporation, accelerating the hydrogen ad-desorption process. The interaction between the two components in the Ni(OH)$_2$/NiMoPO$_x$ further enhances their individual catalytic ability. Therefore, the optimized oxygen incorporated NiMoP catalyst with a thin hydroxide layer modification possesses high reactivities for both water dissociation and hydrogen ad-desorption steps, thus exhibiting a superior HER performance in an alkaline environment. As demonstrated, the optimal Ni(OH)$_2$/NiMoPO$_x$ possesses a remarkable HER activity with a low overpotential of 51 mV at 10 mA cm^{-2} as well as an excellent long-term stability for over 90 h, making it a prominent alternative for Pt-based catalysts. This work provides a direction to design efficient electrocatalysts by strengthening the reactivity of each elementary step.

Conflicts of interest

There are no conflicts to declare.

Acknowledgements

Fig. 5 (a) Chemisorption models of H and OH intermediates on the surfaces of NiMoPO$_x$ and the Ni(OH)$_2$/NiMoPO$_x$ hybrid; calculated adsorption energy diagram of (b) the water dissociation step and (c) hydrogen ad-desorption for Ni(OH)$_2$, NiMoPO$_x$ and the Ni(OH)$_2$/NiMoPO$_x$ hybrid. The symbol * in the sample name represents the active site for DFT calculations. Color codes: Mo, cyan; P, pink; Ni, blue; O, red; H, white.

Notes and references

1 Y. Jiao, Y. Zheng, M. Jaroniec and S. Z. Qiao, *Chem. Soc. Rev.*, 2015, **44**, 2060–2086.
2 I. Roger, M. A. Shipman and M. D. Symes, *Nat. Rev. Chem.*, 2017, **1**, 0003.
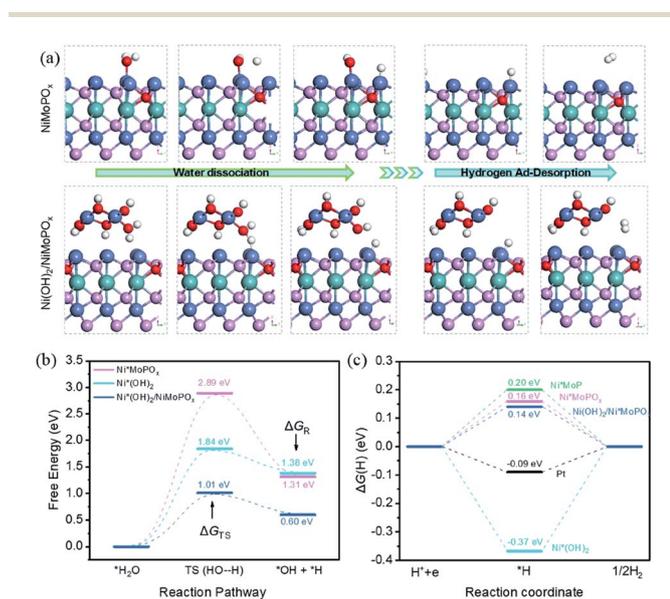3 L. Peng and Z. Wei, *Prog. Chem.*, 2018, 14–28.

4 L. Peng, S. A. S. Syed and Z. Wei, *Chin. J. Catal.*, 2018, **39**, 1575–1593.

5 J. Chi and H. Yu, *Chin. J. Catal.*, 2018, **39**, 390–394.

6 J. R. McKone, S. C. Marinescu, B. S. Brunschwig, J. R. Winkler and H. B. Gray, *Chem. Sci.*, 2014, **5**, 865–878.

7 H. Wang and L. Gao, *Curr. Opin. Electrochem.*, 2018, **7**, 7–14.

8 L. Peng, X. Zheng, L. Li, L. Zhang, N. Yang, K. Xiong, H. Chen, J. Li and Z. Wei, *Appl. Catal., B*, 2019, **245**, 122–129.

9 X. Zhang, F. Zhou, W. Pan, Y. Liang and R. Wang, *Adv. Funct. Mater.*, 2018, 1804600, DOI: 10.1002/adfm.201804600.

10 L. Yang, L. Zeng, H. Liu, Y. Deng, Z. Zhou, J. Yu, H. Liu and W. Zhou, *Appl. Catal., B*, 2019, **249**, 98–105.

11 Y. Huang, J. Hu, H. Xu, W. Bian, J. Ge, D. Zang, D. Cheng, Y. Lv, C. Zhang, J. Gu and Y. Wei, *Adv. Energy Mater.*, 2018, **8**, 1800789.

12 Y. Huang, J. Ge, J. Hu, J. Zhang, J. Hao and Y. Wei, *Adv. Energy Mater.*, 2018, **8**, 1701601.

13 J. Wang, F. Xu, H. Jin, Y. Chen and Y. Wang, *Adv. Mater.*, 2017, **29**, 1605838.

14 L. Peng, Y. Nie, L. Zhang, R. Xiang, J. Wang, H. Chen, K. Chen and Z. Wei, *ChemCatChem*, 2017, **9**, 1588–1593.

15 K. Xiong, L. Li, L. Zhang, W. Ding, L. S. Peng, Y. Wang, S. G. Chen, S. Y. Tan and Z. D. Wei, *J. Mater. Chem. A*, 2015, **3**, 1863–1867.

16 Z. Hao, S. Yang, J. Niu, Z. Fang, L. Liu, Q. Dong, S. Song and Y. Zhao, *Chem. Sci.*, 2018, **9**, 5640–5645.

17 R. Xiang, Y. Duan, L. Peng, Y. Wang, C. Tong, L. Zhang and Z. Wei, *Appl. Catal., B*, 2019, **246**, 41–49.

18 Z. Liu, L. Zhao, Y. Liu, Z. Gao, S. Yuan, X. Li, N. Li and S. Miao, *Appl. Catal., B*, 2019, **246**, 296–302.

19 X. Xiao, L. Tao, M. Li, X. Lv, D. Huang, X. Jiang, H. Pan, M. Wang and Y. Shen, *Chem. Sci.*, 2018, **9**, 1970–1975.

20 L. Su, X. Cui, T. He, L. Zeng, H. Tian, Y. Song, K. Qi and B. Y. Xia, *Chem. Sci.*, 2019, **10**, 2019–2024.

21 Y. Huang, X. Song, J. Deng, C. Zha, W. Huang, Y. Wu and Y. Li, *Appl. Catal., B*, 2019, **245**, 656–661.

22 B. Hinnemann, P. G. Moses, J. Bonde, K. P. Jørgensen, J. H. Nielsen, S. Horch, I. Chorkendorff and J. K. Nørskov, *J. Am. Chem. Soc.*, 2005, **36**, 5308–5309.

23 T. F. Jaramillo, K. P. Jorgensen, J. Bonde, J. H. Nielsen, S. Horch and I. Chorkendorff, *Science*, 2007, **317**, 100–102.

24 A. M. Appel, D. L. Dubois and M. R. Dubois, *J. Am. Chem. Soc.*, 2005, **127**, 12717–12726.

25 P. Xiao, M. A. Sk, L. Thia, X. Ge, R. J. Lim, J. Y. Wang, K. H. Lim and X. Wang, *Energy Environ. Sci.*, 2014, **7**, 2624–2629.

26 A. B. Laursen, S. Kegnæs, S. Dahl and I. Chorkendorff, *Energy Environ. Sci.*, 2012, **5**, 5577–5591.

27 F. Safizadeh, E. Ghali and G. Houlachi, *Int. J. Hydrogen Energy*, 2015, **40**, 256–274.

28 J. Zhang, T. Wang, P. Liu, Z. Liao, S. Liu, X. Zhuang, M. Chen, E. Zschech and X. Feng, *Nat. Commun.*, 2017, **8**, 15437.

29 R. Subbaraman, D. Tripkovic, K. C. Chang, D. Strmcnik, A. P. Paulikas, P. Hirunsit, M. Chan, J. Greeley, V. Stamenkovic and N. M. Markovic, *Nat. Mater.*, 2012, **11**, 550–557.

30 Z. H. Deng, J. Wang, Y. Nie and Z. D. Wei, *J. Power Sources*, 2017, **352**, 26–33.

31 M. Gong, D.-Y. Wang, C.-C. Chen, B.-J. Hwang and H. Dai, *Nano Res.*, 2015, **9**, 28–46.

32 G. Q. Shi and H.-Y. Wang, *Acta Phys.-Chim. Sin.*, 2018, **34**, 22–35.

33 R. L. Doyle, I. J. Godwin, M. P. Brandon and M. E. G. Lyons, *Phys. Chem. Chem. Phys.*, 2013, **15**, 13737–13783.

34 J. Ryu, N. Jung, J. H. Jang, H.-J. Kim and S. J. Yoo, *ACS Catal.*, 2015, **5**, 4066–4074.

35 L. Zhang, X. Wang, X. Zheng, L. Peng, J. Shen, R. Xiang, Z. Deng, L. Li, H. Chen and Z. Wei, *ACS Appl. Energy Mater.*, 2018, **1**, 5482–5489.

36 B. Zhang, J. Liu, J. Wang, Y. Ruan, X. Ji, K. Xu, C. Chen, H. Wan, L. Miao and J. Jiang, *Nano Energy*, 2017, **37**, 74–80.

37 R. Zhang, X. Wang, S. Yu, T. Wen, X. Zhu, F. Yang, X. Sun, X. Wang and W. Hu, *Adv. Mater.*, 2016, **29**, 1605502.

38 J. X. Feng, J. Q. Wu, Y. Tong and G. R. Li, *J. Am. Chem. Soc.*, 2018, **140**, 610–617.

39 Y. Y. Ma, C. X. Wu, X. J. Feng, H. Q. Tan, L. K. Yan, Y. Liu, Z. Kang, E. Wang and Y. G. Li, *Energy Environ. Sci.*, 2017, **10**, 788–798.

40 Y. Yan, B. Y. Xia, X. M. Ge, Z. L. Liu, A. Fisher and X. Wang, *Chem.–Eur. J.*, 2015, **21**, 18062–18067.

41 L. Peng, J. Wang, Y. Nie, K. Xiong, Y. Wang, L. Zhang, K. Chen, W. Ding, L. Li and Z. Wei, *ACS Catal.*, 2017, **7**, 8184–8191.

42 C. Stinner, R. Prins and T. Weber, *J. Catal.*, 2000, **191**, 438–444.

43 D. Boudlich, L. Bih, M. E. H. Archidi, M. Haddad, A. Yacoubi, A. Nadiri and B. Elouadi, *J. Am. Ceram. Soc.*, 2002, **85**, 623–630.

44 P. Hermet, L. Gourrier, J.-L. Bantignies, D. Ravot, T. Michel, S. Deabate, P. Boulet and F. Henn, *Phys. Rev. B: Condens. Matter Mater. Phys.*, 2011, **84**, 235211.

45 J.-L. Bantignies, S. Deabate, A. Righi, S. Rols, P. Hermet, J.-L. Sauvajol and F. Henn, *J. Phys. Chem. C*, 2008, **112**, 2193–2201.

46 M. C. Biesinger, B. P. Payne, L. W. Lau, A. Gerson and R. S. C. Smart, *Surf. Interface Anal.*, 2009, **41**, 324–332.

47 J. W. Lee, T. Ahn, D. Soundararajan, J. M. Ko and J.-D. Kim, *Chem. Commun.*, 2011, **47**, 6305–6307.

48 R. Subbaraman and N. M. Markovic, *Science*, 2011, **334**, 1256.

49 N. Danilovic, R. Subbaraman, D. Strmcnik, K. C. Chang, A. P. Paulikas, V. R. Stamenkovic and N. M. Markovic, *Angew. Chem.*, 2012, **124**, 12663–12666.

50 J. H. Montoya, L. C. Seitz, P. Chakthranont, A. Vojvodic, T. F. Jaramillo and J. K. Nørskov, *Nat. Mater.*, 2016, **16**, 70.

51 T. Liu, X. Ma, D. Liu, S. Hao, G. Du, Y. Ma, A. M. Asiri, X. Sun and L. Chen, *ACS Catal.*, 2016, **7**, 98–102.

52 T. Liu, D. Liu, F. Qu, D. Wang, L. Zhang, R. Ge, S. Hao, Y. Ma, G. Du, A. M. Asiri, L. Chen and X. Sun, *Adv. Energy Mater.*, 2017, **7**, 1700020.